Computers & Fluids 47 (2011) 65–74

Contents lists available at ScienceDirect

Computers & Fluids

journal homepage: www.elsevier.com/locate/compfluid

Filter shape dependence and effective scale separation in large-eddy simulations based on relaxation filtering

J. Berland [a,*], P. Lafon [a], F. Daude [b], F. Crouzet [b], C. Bogey [c], C. Bailly [c]

[a] Laboratoire de Mécanique des Structures Industrielles Durables (LaMSID), UMR CNRS/EDF/CEA 2832, Clamart, France
[b] Électricité de France R&D, Department of Applied Mechanics and Acoustics, Clamart, France
[c] Laboratoire de Mécanique des Fluides et Acoustique (LMFA), École Centrale de Lyon & UMR CNRS 5509, Ecully, France

A R T I C L E   I N F O

Article history:
Received 13 December 2010
Received in revised form 17 February 2011
Accepted 17 February 2011
Available online 2 March 2011

Keywords:
Large-eddy simulation
Explicit filtering
Scale separation
Mixing layer

A B S T R A C T

The influence of the filter shape on the effective scale separation and the numerical accuracy of large-eddy simulations based on relaxation filtering (LES-RF) is investigated. The simulation of the turbulent flow development of a high-Reynolds number low-subsonic compressible mixing layer is performed using the LES-RF procedure, for discrete filters of order 2–10. A reference solution is first obtained using high-order numerical algorithms and shows a good agreement with experimental data found in the literature. Discrete filters of order 2, 4, 6, 8 and 10 are then considered to study the influence of the filter shape on numerical results. The 2nd-order scheme turns out to be too dissipative and prevents the emergence of unsteady motions within the mixing layer. For higher order schemes, from 4th- to 10th-order, the flow solutions are turbulent but exhibit mean flows and turbulent intensities depending on the filter. The investigation of the one-dimensional kinetic energy spectra then shows that the 4th-order filter may still be too dissipative whereas large scales remain unaffected using the 6th-, 8th- and 10th-order filters. A further study of the kinetic energy spectra nonetheless demonstrates that the effective spatial bandwidth of the LES increases with the order of the filtering scheme. Simulations using the 6th-, 8th- and 10th-order filters, with mesh sizes chosen to provide the same effective LES cut-off wavenumber, are performed and yield similar results. It is hence found that the value of the effective LES cut-off wavenumber, rather than to the filter shape itself, is mainly responsible for the discrepancies between the flow statistics obtained using different filters. One may conclude that filter shape independence is consequently achieved in the present LES of a mixing layer.

1. Introduction

Numerical simulations of turbulent motions are capable of providing comprehensive informations on flow fields [16,23]. The relevance of the results obtained might however be affected by the discretization methods, and therefore still has to be carefully examined. Direct numerical simulation (DNS) is so far the most reliable simulation method since the whole range of turbulence scales is resolved and no *a priori* modeling is needed. The use of sufficiently small time steps and mesh sizes ensures on one hand the accuracy of the solution but concurrently dramatically increases the computational cost. Therefore large-eddy simulation (LES) remains to date the prevailing tool for studying realistic high-Reynolds number flow configurations. Low-pass spatial filtering of the turbulent motions allows the computational efforts to focus on the resolution of the largest and most energetic vortical structures while the effect of the scales smaller than the mesh size are taken into account through a subgrid-scale (SGS) model.

Since the early works of Smagorinsky [24], numerous SGS closures have been derived by applying physical assumptions to the filtered Navier–Stokes equations [16]. Reference to the discretization methods is seldom made even though evidences of intricate couplings between the SGS model and the discretization tools have been highlighted [5,17]. Alternatively, some authors, as for instance Boris et al. [10], proposed to employ the truncation errors of the discretization schemes as an implicit SGS model. Within this modeling framework, the dissipation introduced by approximate space differentiation operators is used as a functional model reproducing small scale dissipation. Recent works on this topic include, among others, the approximate local deconvolution model (ALDM) designed by Hickel et al. [18]. For the ALDM, the dissipation introduced by discretization algorithms is locally adjusted to obtain a numerical viscosity consistent with the turbulent viscosity observed for homogeneous isotropic turbulence.

One should nonetheless be very careful when using space discretization schemes exhibiting dissipative properties. Flow

* Corresponding author. Address: EDF R&D, MFEE, I84, 6 Quai Wattier, 78400 Chatou, France.

E-mail address: julien-j.berland@edf.fr (J. Berland).

0045-7930/$ - see front matter © 2011 Elsevier Ltd. All rights reserved.
doi:10.1016/j.compfluid.2011.02.016

anisotropy can indeed be artificially generated and a fine tuning of the dissipation, as achieved by Hickel et al. [18], implies a drastic increase of the complexity of the LES implementation. In addition, the coupling between the numerical methods and the SGS closure alleviates the control over the governing parameters of the LES modeling procedure. This issue can be circumvented by taking into account subgrid dissipation by using an explicit selective filtering of the flow variables. Within the ILES domain, the subfield of explicitly filtered LES is indeed a promising approach. The idea is to minimize the dissipation at the larger scales while diffusing through the smaller scales the drain of energy due to the turbulence energy cascade. When using low-dissipation or even purely dispersive schemes, such as centered finite differences, the filtering alone is connected to the subgrid-scale activity and the modeling efforts focus on the features of the filtering procedure only. Stolz and Adams [25], Mathew et al. [20], Tantikul and Domaradzki [27], Domaradzki [13] as well as Bogey and Bailly [7] designed such SGS models. In the recent works of Bogey and Bailly [8], a detailed description of the methodology, referred to as LES based on relaxation filtering (LES-RF) by the authors, can be found.

Since LES-RF requires to explicitly perform scale separation, it raises the question of the choice of the filter. LES theoretical framework imposes few constraints on its properties: its cut-off wavenumber should lie in the inertial range but its shape can be *a priori* freely chosen. Some studies have been carried out to evaluate the impact of the choice of the filter on SGS modeling [4,11,12,19]. In particular, Berland et al. [4] demonstrated by using the EDQNM theory that filters with sharp cut-off are more appropriate for LES since they result in a clear separation between resolved and unresolved scales. It was also shown that for the second-order filter, which has a smoothly graded transfer function, the SGS tensor does no longer truly represent interactions between scales of the inertial range so that the universality assumption is no longer fulfilled. Similar results, supporting the need of using sharp cut-off filters, have been obtained by De Stefano and Vasilyev [12] for the filtered Burger's equation. These guidelines have been obtained from studies of incompressible canonical flows and it may be valuable to now extend these observations to more realistic turbulent configurations. In particular, compressible flows are of special interest as the use of LES-RF in this community is spreading [3,8,9,15,20,22].

The aim of the present study is then to investigate the influence of the filter shape on compressible LES based on relaxation filtering. The flow configuration is a low subsonic shear layer. Plane mixing layers have been greatly studied because of their relative simplicity in one hand, and because their development are usually characterized by a flow scenario occurring in many configurations, consisting of a laminar breakdown, followed by the emergence of large scale coherent structures then leading to a fully turbulent state. The compressible LES-RF of a spatially developing turbulent mixing layer, with Reynolds number $\mathrm{Re}_{\delta_{\omega_0}} = \delta_{\omega_0} U_c/\nu = 5 \times 10^4$ based on the convection velocity U_c and the initial vorticity thickness δ_{ω_0}, has been performed with this aim in view using the solver *Code_Safari* [14]. Discrete filters of orders from 2 to 10 have been implemented to describe the way in which they can affect the solution. Extensive comparisons have been carried out between the mean flow, the turbulent intensities and the velocity spectra obtained for each filter shape. The issue of scale separation, related to the effective LES cut-off wavenumber, has also been studied based on turbulent kinetic energy spectra. The result analysis has been complemented by a discussion on the possibility of filter independence in LES-RF with the aim of determining whether the discrepancies observed between the simulations are related to the filter shape itself or to the effective LES cut-off wavenumber.

The parameters of the simulation are first described in Section 2. A reference mixing layer solution, obtained using high-order numerical algorithms, is proposed in Section 3. An investigation of the influence of the filtering shape is then carried out in Section 4. Concluding remarks are finally drawn in Section 5.

2. Simulation apparatus

2.1. Numerical methods and subgrid-scale modeling

The compressible Navier–Stokes equations, as formulated by Vreman et al. [29], are solved using high-order numerical schemes. To take account of the dissipation provided by the unresolved scales, a LES based on relaxation filtering (LES-RF) is performed [8]. An explicit spectral-like filtering is therefore applied to the conservative flow variables: the density ρ, the three components of the velocity momentum ρu_i and the total energy ρe. The method has been successfully used in various applications [3,7].

Approximate derivatives are evaluated using low-dispersion 4th-order 11-point explicit finite differences [6] whose properties have been optimized in the Fourier space. Explicit filtering is performed thanks to centered standard discrete filters [28] whose order ranges from 2 (3-point stencil) to 10 (11-point stencil). Time integration is carried out by an optimized fourth-order low-storage Runge–Kutta scheme [2].

The calculation carried out using the 10th-order filter, which exhibits the sharpest spectral cut-off, will be considered to provide the reference solution.

2.2. Simulation parameters

A high-Reynolds number low-subsonic mixing layer is considered. As an illustration, a sketch of the computational domain and of the coordinate system is provided in Fig. 1. The initial conditions are defined by an hyperbolic-tangent velocity profile

$$u(y) = \frac{U_1 + U_2}{2} + \frac{U_2 - U_1}{2} \tanh\left(\frac{2y}{\delta_{\omega_0}}\right) \qquad (1)$$

where the two freestream velocities are given by $U_1 = 50\ \mathrm{m\,s^{-1}}$ and $U_2 = 100\ \mathrm{m\,s^{-1}}$, so that the convective velocity is equal to $U_c = (U_1 + U_2)/2 = 75\ \mathrm{m\,s^{-1}}$, corresponding to a convective Mach number $M_c = 0.22$. The initial vorticity thickness of the sheared

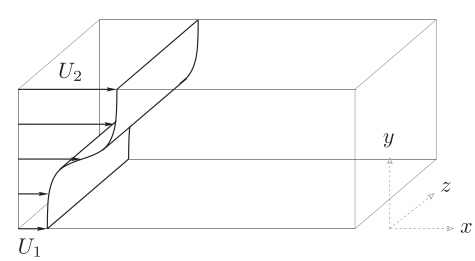

Fig. 1. Sketch of the computational domain and of the coordinate system (the figure is not to scale).

Table 1
Coefficients of the standard discrete filters of order 2, 4, 6, 8 and 10. Coefficients with negative indices may be retrieved using the relationship $d_{-j} = d_j$.

$2N+1$	3 $\left(d_j^{3s}\right)$	5 $\left(d_j^{5s}\right)$	7 $\left(d_j^{7s}\right)$	9 $\left(d_j^{9s}\right)$	11 $\left(d_j^{11s}\right)$
d_0	1/2	3/8	5/16	35/128	63/256
d_1	−1/4	−1/4	−15/64	−7/32	−105/512
d_2		1/16	3/32	7/64	15/128
d_3			−1/64	−1/32	−45/1024
d_4				1/256	5/512
d_5					−1/1024

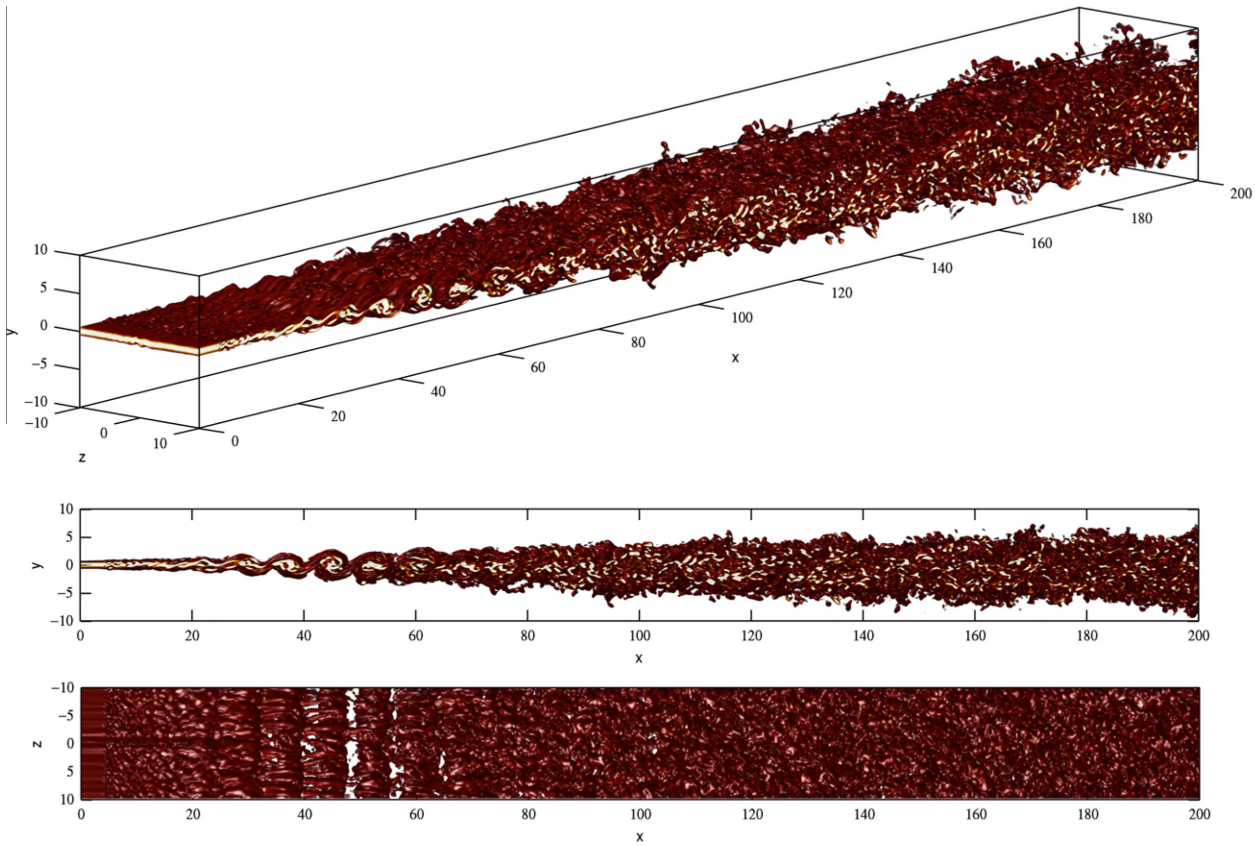

Fig. 2. Snapshot of the spanwise vorticity component $\omega_z\delta_{\omega_0}/U_c$ in the whole computational domain obtained for the 10th-order standard filters. Colorscale from -0.5 (red) to -0.2 (white). From top to bottom: isometric view, side view, top view (coordinates are normalized by the initial vorticity thickness δ_{ω_0}). (For interpretation of the references to color in this figure legend, the reader is referred to the web version of this article.)

region is equal to $\delta_{\omega_0} = 10^{-2}$ m. The Reynolds number is then $\mathrm{Re}_{\delta_{\omega_0}} = \delta_{\omega_0}U_c/\nu = 5 \times 10^4$.

The calculation domain is discretized using $N_x \times N_y \times N_z = 950 \times 261 \times 101 \simeq 25 \times 10^6$ nodes distributed on a structured Cartesian grid and has physical dimensions of $[0, 200\delta_{\omega_0}] \times [-90\delta_{\omega_0}, 90\delta_{\omega_0}] \times [-10\delta_{\omega_0}, 10\delta_{\omega_0}]$. Within the turbulent flow region the mesh size is uniform with $\Delta y = \delta_{\omega_0}/8$ and $\Delta x = \Delta z = \delta_{\omega_0}/5$. Further away from the shear layer, the grid is stretched in the y direction to provide a large extent of the domain in this direction while keeping the computational cost at a reasonable level. The calculation domain is periodic in the z direction. The non-reflecting boundary conditions of Tam and Dong [26] are specified at the boundaries of the domain. The time step $\Delta t \simeq 3 \times 10^{-6}$ s corresponds to a Courant–Friedrichs–Lewy number equal to 0.8. To ensure statistical convergence of the flow, the simulation is run over approximately 10 flow through times, corresponding to 10^5 iterations.

2.3. Turbulence ignition by flow excitation

To seed the laminar breakdown of the mixing layer, the flow is excited at the upstream boundary of the calculation domain. An harmonic forcing at the most unstable frequency f_h of the mixing layer is introduced, while random fluctuations are also added to ensure a transition to a fully three dimensional turbulent regime further downstream. Velocity fluctuations, referred to as u_e, v_e and w_e, are hence artificially introduced at every time step in the following way:

$$\begin{pmatrix} u_e \\ v_e \\ w_e \end{pmatrix} = \begin{pmatrix} U_r\varepsilon_u \\ U_r\varepsilon_v + U_h\sin(2\pi f_h t) \\ U_r\varepsilon_w \end{pmatrix} \cdot S(x,y,t) \tag{2}$$

where $S(x,y,t)$ is a shape factor which reads

$$S(x,y,t) = \exp\left[-\log(2)\frac{(x-x_0)^2 + (y-y_0)^2}{b^2}\right] \tag{3}$$

The quantities ε_u, ε_v and ε_w are random variables uniformly distributed on the interval $[-1, 1]$. These variables introduce random motions on the three velocity components. Their magnitude is given by U_r so that $U_r/U_c = 5 \times 10^{-2}$. Concerning the harmonic forcing, it is only applied to the transverse velocity component v. Its amplitude is so that $U_h/U_c = 10^{-3}$. The excitation frequency f_h can be deduced from a linear stability analysis [21] and is equal to

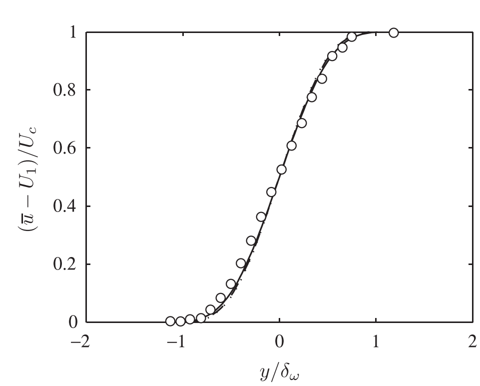

Fig. 3. Mean streamwise velocity $\bar{u}$ as a function of the transverse location y/δ_ω obtained for the 10th-order standard filters, for various streamwise locations. ——, $x/\delta_{\omega_0} = 100$; - - -, $x/\delta_{\omega_0} = 120$; ·······, $x/\delta_{\omega_0} = 140$; ○, experimental data of Bell and Mehta [1].

$$f_h = 0.132\frac{U_c}{\delta_{\omega_0}} \tag{4}$$

Finally, the shape factor S allows to apply the excitation only over a limited flow region. The magnitude is modulated in space by a Gaussian function equal to 1 when $(x, y) = (x_0, y_0) = (5\delta_{\omega_0}, 0)$ and for any spanwise location z. Away from the line (x_0, y_0, z) the amplitude decreases and eventually reaches zero. The half-width of the shape factor is related to the parameter b, here chosen to be equal to $\delta_{\omega_0}/2$.

2.4. Filter shape modification

Applying a central, $2N+1$ point stencil discrete filter on a uniform mesh in the x-direction reads as

$$\bar{f}(x) = f(x) - \sigma\sum_{j=-N}^{N} d_j f(x + j\Delta x) \tag{5}$$

where d_j are the scheme coefficients and Δx the mesh size [28]. The same scheme is applied sequentially in the three directions x, y and z. The filtering strength σ is set to 0.4 in the present simulations.

To avoid any interplay between the filter shape and the flow excitation at the inlet, the 11-point 10th-order selective filter has been used in all simulations in the upstream region of the calculation domain, for $x/\delta_{\omega_0} < 25$. Further downstream, for $x/\delta_{\omega_0} > 50$, different filters based on 3-, 5-, 7- and 9-point stencils have been employed. In the intermediate region, when $25 < x/\delta_{\omega_0} < 50$, a linear transition between the sets of coefficients used upstream and downstream is achieved to provide a smooth transition between the two filter shapes. The coefficients d_j of the discrete filter are therefore defined as

$$d_j(x) = [1 - \chi(x)]d_j^{\text{upstream}} + \chi(x)d_j^{\text{downstream}} \tag{6}$$

where the function $\chi(x)$ is given by

$$\chi(x) = \begin{cases} 0 & \text{if } x/\delta_{\omega_0} < 25 \\ (x-25)/25 & \text{if } 25 < x/\delta_{\omega_0} < 50 \\ 1 & \text{if } x/\delta_{\omega_0} > 50 \end{cases} \tag{7}$$

Five calculations have been carried out. For all of them, the upstream filter is the 10th-order 11-point scheme, so that $d_j^{\text{upstream}} = d_j^{11s}$, which are given in Table 1. The reference solution based on the 10th-order filter is such as $d_j^{\text{upstream}} = d_j^{\text{downstream}} = d_j^{11s}$. The influence of the filter shape has then been studied by modifying the set of coefficients used for $d_j^{\text{downstream}}$. For the simulations with discrete filters of 2nd-, 4th-, 6th- and 8th-order, the coefficients $d_j^{\text{downstream}}$ are respectively set to the value given $d_j^{3s}, d_j^{5s}, d_j^{7s}, d_j^{9s}$, which are given in Table 1.

Remind that the finite difference scheme is the same for all the calculations. Only the influence of the filtering is therefore investigated in the present work.

3. Reference simulation

3.1. Unsteady flow field

A snapshot of the spanwise vorticity $\omega_z\delta_{\omega_0}/U_c$ in the whole calculation domain is provided in Fig. 2. The flow pattern is typical of a spatially developing mixing layer. In the laminar flow region ($x/\delta_{\omega_0} < 5$), instabilities are growing, leading to the roll-up of the mixing interface responsible for the emergence of large-scale organized structures, whose size are comparable with the transverse length scale of the flow. Such vortices are for instance clearly visible around $x/\delta_{\omega_0} = 50$. Further downstream, for about $x/\delta_{\omega_0} > 100$, the flow reaches a fully turbulent state with a large range of motion scales, especially fine structures characterizing high-Reynolds number flows.

3.2. Mean flow results

The consistency of the mean flow field is now investigated. Comparisons to experimental data are performed at three streamwise locations, $x/\delta_{\omega_0} = 100$, $x/\delta_{\omega_0} = 125$ and $x/\delta_{\omega_0} = 150$, in the fully turbulent region.

The transverse profiles of the mean normalized streamwise velocity $(\bar{u} - U_1)/U_c$ are plotted in Fig. 3 as functions of the transverse location y normalized by the local vorticity thickness δ_ω. The experimental data of Bell and Mehta [1] are also represented. It is seen that the LES velocity profiles perfectly collapse, demonstrating that the mean flow is self-similar in the downstream region of the calculation domain. The agreement between numerical and experimental data is in addition good.

Further comparisons are carried out in Fig. 4 where the turbulent intensities, $\overline{u'u'}^{1/2}$, $\overline{v'v'}^{1/2}$ and $\overline{w'w'}^{1/2}$ are represented as

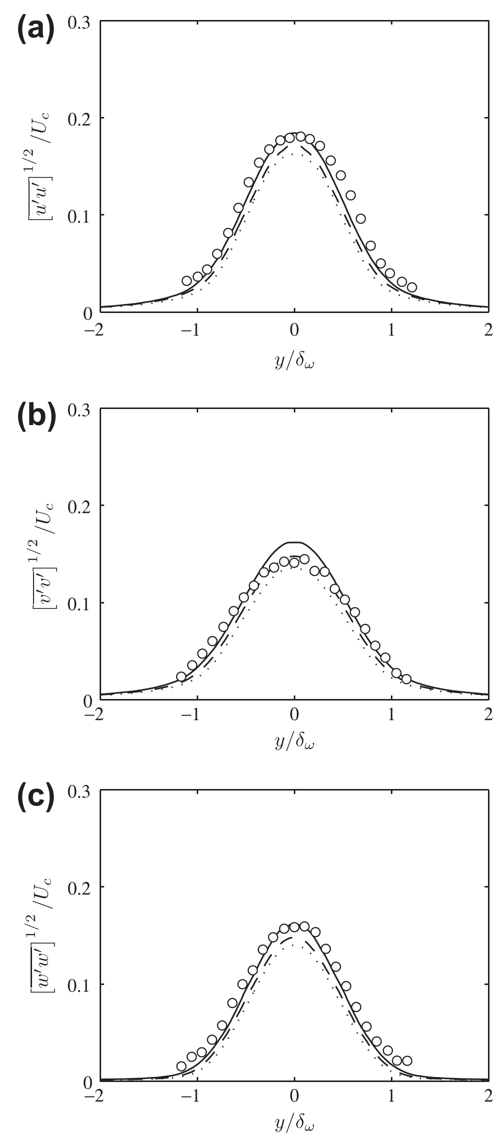

Fig. 4. Turbulent intensities as functions of the transverse location y/δ_ω obtained for the 10th-order standard filters, for various streamwise locations. ——, $x/\delta_{\omega_0} = 100$; – – –, $x/\delta_{\omega_0} = 120$; ·······, $x/\delta_{\omega_0} = 140$; ∘, experimental data of Bell and Mehta [1]. Turbulent intensities based on: (a) the streamwise, (b) the transverse, and (c) the spanwise velocity components.

functions of the transverse location y, for the three streamwise locations: $x/\delta_{\omega_0} = 100$, $x/\delta_{\omega_0} = 125$ and $x/\delta_{\omega_0} = 150$. The measurements of Bell and Mehta [1] are also presented. The LES profiles all exhibit a Gaussian shape centered on the mixing layer centerline ($y/\delta_\omega = 0$) where turbulent activity is the most intense. They are in rather good agreement with the experimental results, despite few discrepancies in amplitude. The half-width of the transverse profiles are in particular accurately reproduced by the simulations.

4. Filter shape influence

4.1. Numerical results

4.1.1. Overview of the flow field

Snapshots of the modulus of the spanwise vorticity component $|\omega_z|\delta_{\omega_0}/U_c$ taken in the central plane of the computational domain are presented in Fig. 5 for the 2nd-, 4th-, 6th-, 8th- and 10th-order discrete filters.

It is first observed that for the 2nd-order filter, turbulence ignition is damped. The mixing layer indeed goes back to a laminar state as the 2nd-order filter is applied, which indicates that the filter introduced far too much dissipation. This filter therefore seems to be inappropriate for the simulation of the present turbulent flow. In the remainder of the paper, reference to the data obtained with the 2nd-order filter will then no longer be made.

For the filters of orders ranging from 4 to 10, turbulence is observed to develop, leading to the emergence of unsteady motions. As expected, the solutions determined using the different filters are distinct since large-eddy simulations yield a filtered velocity field which is intrinsically dependent on the choice of the filter. When the order is increased from 4 to 10, from Fig. 5b to e, a broadening of the resolved scale bandwidth is clearly visible. It is worth noting that the four snapshots of the flow field show strong similarities. In all cases, coherent vortical structures are generated around $x/\delta_{\omega_0} = 25$, vortex breakdown and flow three-dimensionalization is observed in the neighborhood of $x/\delta_{\omega_0} = 80$, and a fully turbulent state is eventually reached for $x/\delta_{\omega_0} > 150$. This suggests that even though the solutions are different, the key elements of the flow physics are reproduced in a similar manner using the 4th-, 6th-, 8th- and 10th-order filtering schemes.

4.1.2. Mean and turbulent flow quantities

To first check that the modifications of the filter shape in the streamwise direction, as described in Section 2.4, has a weak impact on the early development of the flow field, the turbulent intensities $[\overline{u'u'}]^{1/2}$, $[\overline{v'v'}]^{1/2}$ and $[\overline{w'w'}]^{1/2}$ are represented as functions of the streamwise location x in Fig. 6a, b and c. It is observed

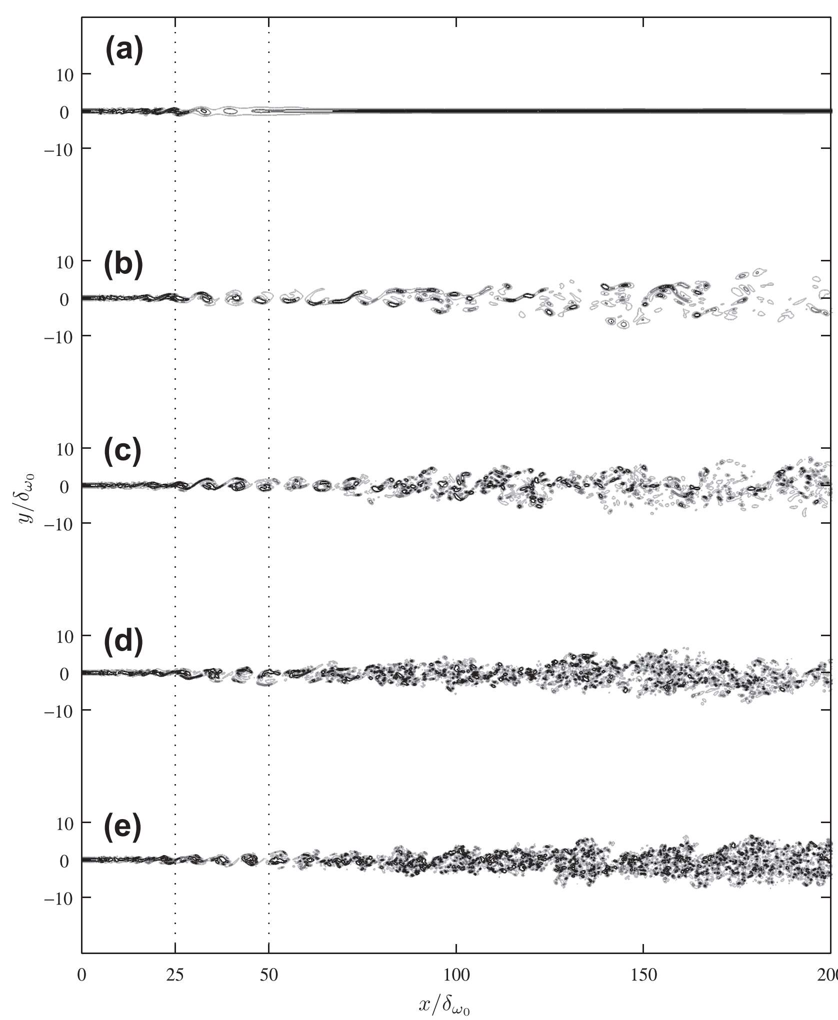

Fig. 5. Snapshot of the modulus of the spanwise vorticity component $|\omega_z|\delta_{\omega_0}/U_c$ in the central plane of the computational domain obtained for various discrete filters downstream of $x/\delta_{\omega_0} = 50$. Colorscale from 0 (white) to 0.5 (black). (a) 2nd-order; (b) 4th-order; (c) 6th-order; (d) 8th-order; (e) 10th-order filter. The vertical dotted lines indicate the transition region between the upstream and downstream filterings.

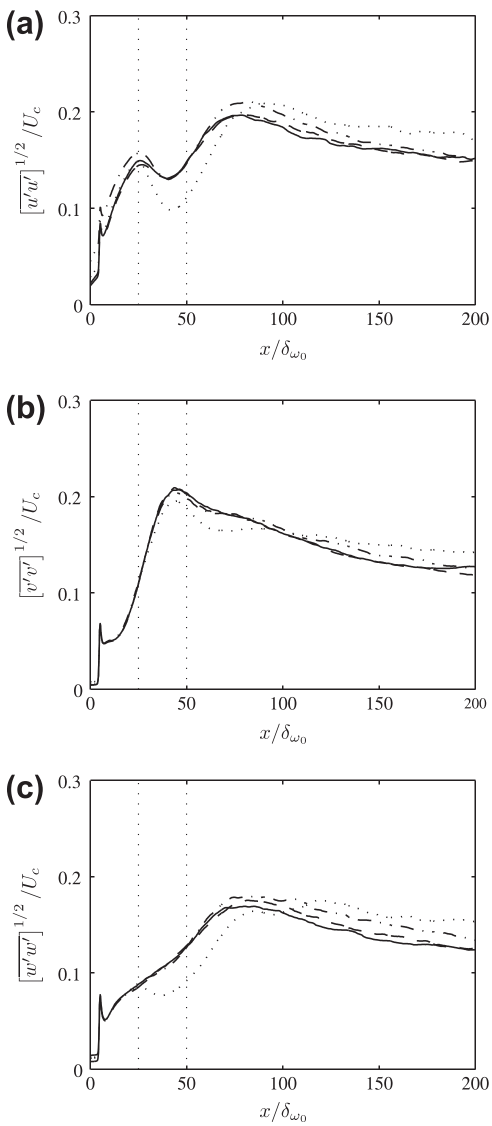

Fig. 6. Turbulent intensities on the mixing layer centerline as functions of the streamwise location x/δ_{ω_0} for various discrete filters downstream of $x/\delta_{\omega_0} = 50$. ······, 4th-order; –.–.–, 6th-order; – – –, 8th-order; ——, 10th-order. Turbulent intensities based on: (a) the streamwise, (b) the transverse, and (c) the spanwise velocity components. The vertical dotted lines indicate the transition region between the upstream and downstream filterings.

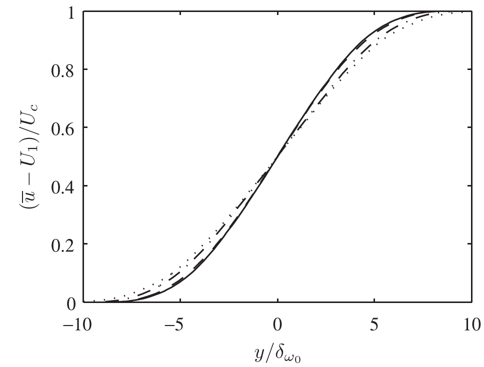

Fig. 7. Mean streamwise velocity $\overline{u}$ as a function of the transverse location y/δ_{ω_0} at $x/\delta_{\omega_0} = 175$, for various discrete filters. ······, 4th-order; –.–.–, 6th-order; – – –, 8th-order; ——, 10th-order.

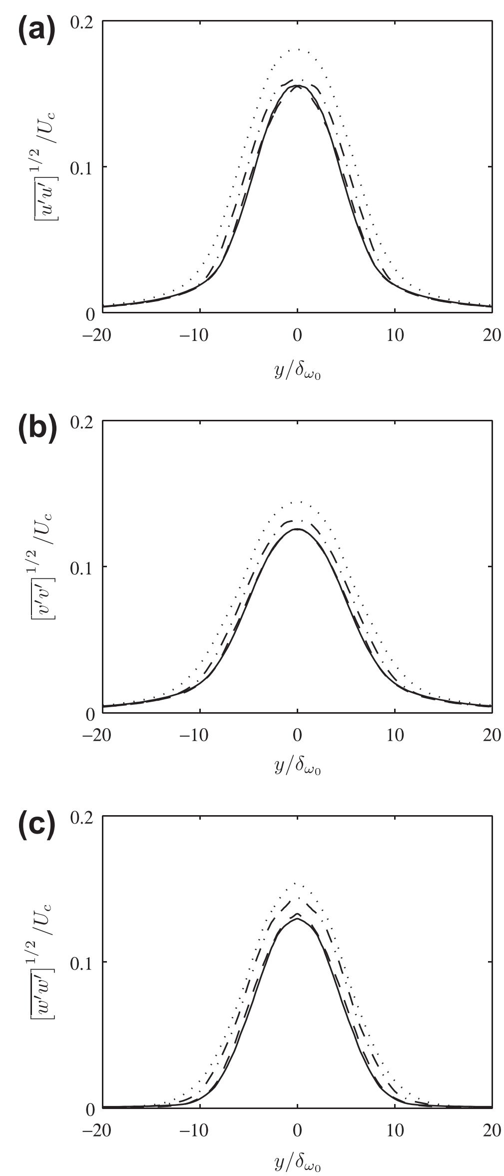

Fig. 8. Turbulent intensities as functions of the transverse location y/δ_{ω_0} at $x/\delta_{\omega_0} = 175$, for various discrete filters. ······, 4th-order; –.–.–, 6th-order; – – –, 8th-order; ——, 10th-order. Turbulent intensities based on: (a) the streamwise, (b) the transverse, and (c) the spanwise velocity components.

that the turbulent intensities indeed collapse well in the upstream region of the calculation, for $x/\delta_{\omega_0} < 25$, even though a slight overestimation of the streamwise component $\overline{[u'u']}^{1/2}$ is visible for the 6th-order filter.

In the transition area, for $25 < x/\delta_{\omega_0} < 50$, the turbulence levels obtained for the 4th-order filter are underestimated and this trend permeates down to $x/\delta_{\omega_0} = 75$. Further downstream, the turbulent intensities predicted using the 4th-order scheme are larger than those of the reference data obtained using the 10th-order filter. The results corresponding to the 6th-order filter exhibit a similar behavior, whereas smaller discrepancies can be seen between the solutions calculated using the 8th- and the 10th-order filtering algorithms.

Mean flow quantities obtained in the fully turbulent region are now investigated. The transverse profiles of the mean streamwise velocity at $x/\delta_{\omega_0} = 175$ are plotted in Fig. 7 for the various standard filters. A good collapse of the profiles obtained using the 8th- and 10th-order filter is seen. Using the 4th- and 6th-order filters, the velocity gradient in the sheared region is significantly smoother.

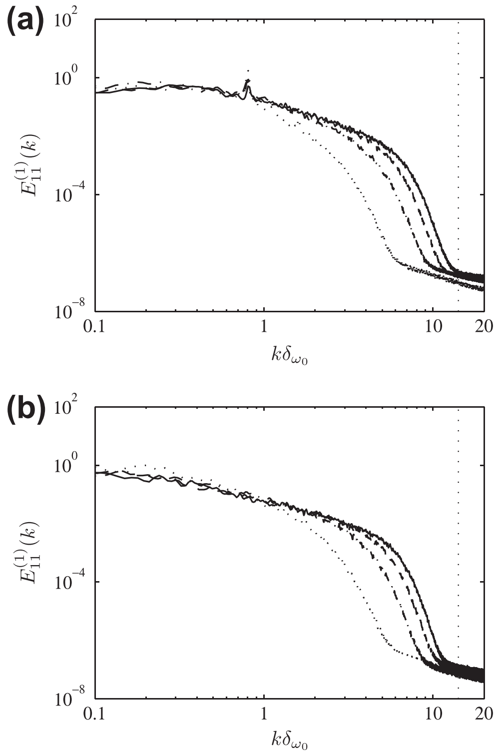

Fig. 9. One-dimensional turbulent kinetic energy spectrum $E_{11}^{(1)}(k)$, evaluated at several streamwise locations on the mixing layer centerline for various discrete filters. ⋯⋯, 4th-order; –.–.–, 6th-order; – – –, 8th-order; ——, 10th-order. (a), $x/\delta_{\omega_0} = 75$; (b), $x/\delta_{\omega_0} = 175$. The vertical dotted line represents the mesh cut-off wavenumber $k_c = \pi/\Delta x$ in the streamwise direction.

This trend is further confirmed by the transverse profiles of the turbulent intensities $\overline{[u'u']}^{1/2}$, $\overline{[v'v']}^{1/2}$ and $\overline{[w'w']}^{1/2}$ measured at $x/\delta_{\omega_0} = 175$ and presented in Fig. 8a, b and c. The 8th- and 10th-order filters indeed exhibit very similar profiles whereas the lower order filters overestimate the turbulence activity.

4.1.3. Velocity spectra

Using Taylor's assumption of frozen turbulence, point-wise measurements of the turbulent motions has allowed us to determine the one-dimensional kinetic energy spectrum $E_{11}^{(1)}(k)$, in the x direction, based on the streamwise velocity perturbations u'. For the filters of order 4–10, spectra measured on the mixing layer centerline ($y/\delta_{\omega_0} = 0$, where turbulence activity reaches its maximum amplitude) are displayed in Fig. 9a and b for the two locations $x/\delta_{\omega_0} = 75$ and $x/\delta_{\omega_0} = 175$, respectively. Remark that because the present spectra are evaluated using point-wise time-resolved data, the spectral content can lie above the grid cut-off wavenumber $k_c = \pi/\Delta x$ which is represented in Fig. 9a and b by a dotted line.

In the transitional flow region, for $x/\delta_{\omega_0} = 75$, the spectra all exhibit a similar shape. A peak at $k\delta_{\omega_0} \sim 0.8$, emerges and corresponds to coherent vortical structures whose formations have been triggered by the upstream harmonic flow excitation. For higher wavenumbers, above $k\delta_{\omega_0} = 1$, a strong decrease of the kinetic energy is visible. As already pointed out in Section 4.1.1, a broadening of the kinetic energy spectrum is observed when the order of the filter increases.

Further downstream, at $x/\delta_{\omega_0} = 175$ in Fig. 9b, the spectra obtained for the 6th-, 8th- and 10th-order filters exhibit a good collapse for the large scales corresponding to wavenumbers $k\delta_{\omega_0} < 1$. At this location, where the flow field is fully turbulent, a well-defined inertial range is also visible, with an extent increasing with the order of the filter. The inertial range lies for instance over the interval $0.1 < k\delta_{\omega_0} < 2$ for the 6th-order scheme whereas it is observed up to about $k\delta_{\omega_0} = 5$ for the 10th-order filter. Above these wavenumbers, small scales are dissipated by the filtering procedure and a steep decrease of the energy is seen.

Concerning the spectrum provided by the simulation with the 4th-order filter, it is different from those obtained by higher-order filters. In particular, a peak is visible for $k\delta_{\omega_0} \sim 0.2$ and the slope of the inertial range is higher. These modifications of the flow development are probably due to the fact that the 4th-order discrete filter is more dissipative and then leads to a lower effective LES cut-off. The dynamics of large-scale motions is also likely to be perturbed by the excessive unwanted dissipation introduced by the filter. Note that the space and time discretization schemes may have an influence on scale-separation but this point has not been further investigated.

At this point, according to the kinetic energy spectra presented here, it seems that varying the order of the filter from 6 to 10 has a low impact on the dynamics of the larger scales. In that case, increasing the order of the scheme indeed apparently mainly shifts the effective cut-off wavenumber of the simulation towards the grid cut-off. Based on these results, the discrepancies observed between the different filters may be mainly related to the effective spatial bandwidth of the LES, rather than to the filter shape itself. The validity of this assumption is discussed in Section 4.3 but the effective cut-off wavenumber of the LES first needs to be defined and evaluated.

4.2. Scale separation

As shown by the velocity spectra presented in Section 4.1.3 the various simulations provide solutions characterized by different cut-off wavenumbers depending on the order of the filter. A decomposition into filtered and unfiltered scales is performed here

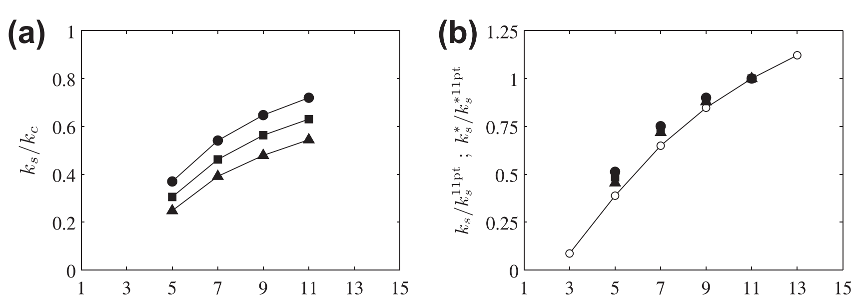

Fig. 10. (a) Effective LES cut-off wavenumber k_s. (b) Normalized effective LES cut-off wavenumber $k_s/k_s^{11\mathrm{pt}}$ and filter cut-off wavenumber $k_s^*/k_s^{*11\mathrm{pt}}$ for the standard discrete filters as functions of the number of points $2N+1$ of the algorithm (cut-off wavenumbers are normalized by the value obtained for the 11-point scheme). ∘, filter cut-off wavenumber; ▲, ■, •, effective LES cut-off wavenumber for $A = 10^{-4}$, $A = 10^{-5}$ and $A = 10^{-6}$.

by introducing an arbitrary criterion on the amplitude of the kinetic energy spectrum: it is assumed that wavelengths having a small contribution to the turbulent activity correspond to filtered scales.

The effective LES cut-off wavenumber is here defined as the wavenumber k_s above which the kinetic energy spectrum $E_{11}^{(1)}(k)$ is smaller than an arbitrary value A. Estimations of k_s are made at the location $x/\delta_{\omega_0} = 175$ where a fully turbulent state is observed. For the amplitude threshold A, it seems reasonable to take a value larger than the magnitude of the residual background noise, seen for $k\delta_{\omega_0} > 10$, and smaller than the amplitude of well-resolved scales, typically with $k\delta_{\omega_0} < 1$. For sake of completeness, three thresholds have been tested: $A = 10^{-4}$, $A = 10^{-5}$, $A = 10^{-6}$. The resulting effective cut-off wavenumbers k_s are plotted in Fig. 10a against the number of points $2N + 1$ of the filter. As expected, the spatial resolution bandwidth increases with the order of the filter. Another predictable result is that the values of the cut-off wavenumber k_s depend on the choice of the threshold A. However, rather than using the value of k_s itself, it may be more relevant to evaluate the variations of the effective scale separation from one filter to another. In Fig. 10b, the cut-off wavenumber k_s has been normalized by the value obtained for the 10th-order filter (for the same threshold A). The LES effective cut-off wavenumbers then almost collapse for the three threshold values of A, hence demonstrating the robustness of the proposed indicator.

An *a posteriori* evaluation of the effective LES cut-off is a matter of interest but it may also be interesting to have *a priori* indicators that can be easily computed solely from the knowledge of the filter shape. Bogey and Bailly [6] proposed to defined the filter cut-off $k^*\Delta x$ using the following criterion on the transfer function: let $k^*\Delta x$ be the smallest wavenumber such as $1 - G(k\Delta x) \geqslant 2.5 \times 10^{-3}$, with the filter response G given by

$$G(k\Delta x) = 1 - d_0 - \sum_{j=1}^{N} 2d_j \cos(jk\Delta x) \tag{8}$$

where d_j are the coefficients of the filter. The values obtained for the cut-off $k^*\Delta x$ are compared in Fig. 10b to those deduced from the LES kinetic energy spectra. Note that the results have been normalized by the cut-off wavenumber of the 11-point algorithm. A good agreement is found between the two sets of data. The effective scale separation is therefore clearly shown to be directly related to the dissipation properties of the filter and relative increases or decreases of the LES cut-off wavenumber can be known using only the filter transfer function.

4.3. Filter shape independence

The choice of the filter clearly has an influence on LES flow fields. The investigation of the effective scale separation carried out in Section 4.2 also demonstrates that the LES cut-off wavenumber vary with the filter shape. Therefore, to truly verify whether filter independence is achieved in the present LES-RF of mixing layers, comparisons must be made between calculations having the same cut-off wavenumber. In that case, the comparisons of the solutions obtained using different filters must be made for mesh sizes adjusted so as to fix scale separation at the same wavenumber. Based on the criterion of Bogey and Bailly [6], the ratio between the cut-off wavenumbers of the 10th- and 6th-order filters is equal to 1.51, and it is equal to 1.31 when considering the 8th- and 6th-order schemes. Consequently a simulation performed using a 6th-order filter on the reference grid used so far should have the same effective LES cut-off wavenumber as the one obtained using a 10th-order filter on a grid 1.51 times coarser or using a 8th-order filter on a grid 1.31 coarser. The two latter calculations have been carried out, and their solutions have been compared to the former simulation using 6th-order filtering. In these calculations, since the mesh size changes, no attempt has been made to ensure that the flow excitation is the same for all the simulations. The same filter is applied to the whole domain and the procedure described in Section 2.4 is not implemented. Quantitative comparisons are consequently only performed in the turbulent region.

Qualitative comparisons between the three simulations are first proposed in Fig. 11 where instantaneous vorticity field are plotted in the central plane of the computational domain, for the 6th-order filter (fine mesh) and the 8th- and 10th-order filters (coarser meshes). The three calculations, even though they have been

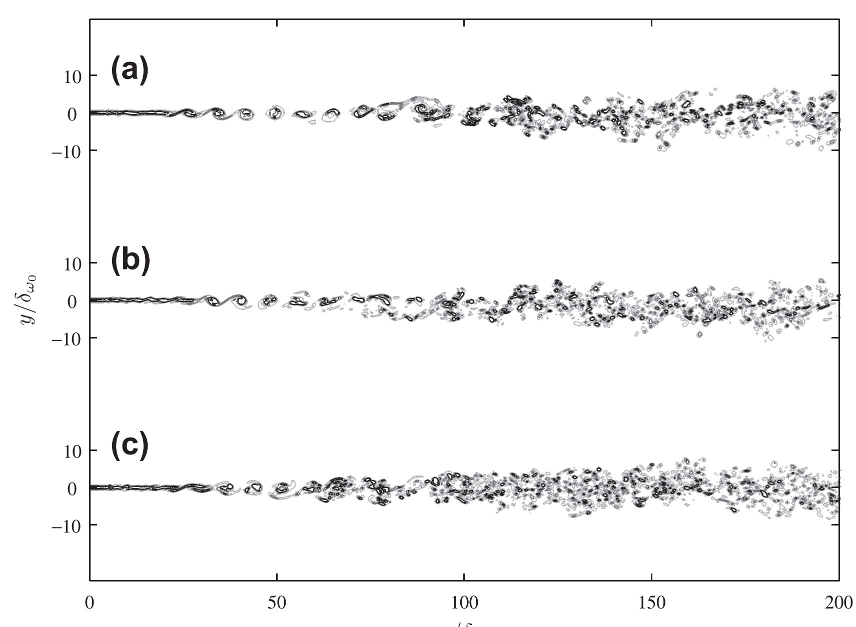

Fig. 11. Snapshot of the modulus of the spanwise vorticity component $|\omega_z|\delta_{\omega_0}/U_c$ in the central plane of the computational domain obtained for various discrete filters with adjusted mesh size to provide the same effective LES cut-off wavenumber. Colorscale from 0 (white) to 0.5 (black). (a), 6th-order (fine mesh); (b), 8th-order (coarse mesh); (c), 10th-order (coarse mesh).

performed on different grids with different filters, provide similar turbulent mixing layer developments. In particular, in the developed flow region for $x/\delta_{\omega_0} > 150$, the flow and the spatial bandwidth seem to agree well in all simulations.

These observations are further supported by quantitative comparisons. The turbulent intensities $[\overline{u'u'}]^{1/2}$, $[\overline{v'v'}]^{1/2}$ and $[\overline{w'w'}]^{1/2}$, measured at $x/\delta_{\omega_0} = 175$ are presented in Fig. 12a, b and c, for the 6th-order filter (fine mesh) and the 8th- and 10th-order filters (coarser meshes). A satisfactory agreement is obtained for the three turbulent intensity components given here even though variations are visible for the transverse intensity in Fig. 12b on the mixing layer centerline. It should be noted that the resolution bandwidth of the differentiation schemes is narrower using coarser grids, which might lead to a loss of accuracy. The agreement remains nonetheless very good for $[\overline{u'u'}]^{1/2}$ and $[\overline{w'w'}]^{1/2}$.

The investigation of the one-dimensional kinetic energy spectra $E_{11}^{(1)}(k)$ confirms the present findings. The spectra $E_{11}^{(1)}(k)$ measured at $x/\delta_{\omega_0} = 175$ for 6th-order filter (fine mesh) and the 8th- and 10th-order filters (coarser meshes) is depicted in Fig. 13. They collapse very well. For the unfiltered scales in particular, for $k\delta_{\omega_0} < 3$, the spectra exhibit similar magnitudes and the effective cut-off appears to be the same for all three calculations.

Consequently the present flow solutions seem to mainly depend on the effective LES cut-off wavenumber rather than on the filter shape itself, which indicates that filter shape independence is here achieved for the 6th-, 8th- and 10th-order filters.

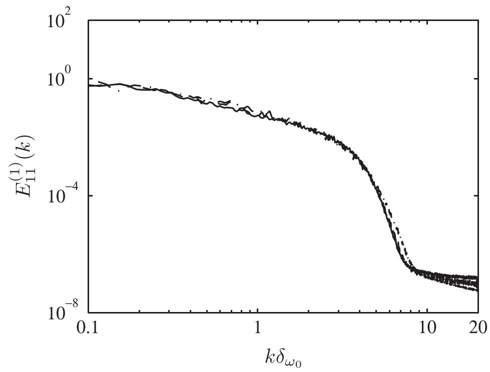

Fig. 13. One-dimensional turbulent kinetic energy spectrum $E_{11}^{(1)}(k)$, evaluated at $x/\delta_{\omega_0} = 175$ on the mixing layer centerline for various discrete filters with adjusted mesh size to provide the same effective LES cut-off wavenumber. –.–.–, 6th-order; – – –, 8th-order; ——–, 10th-order.

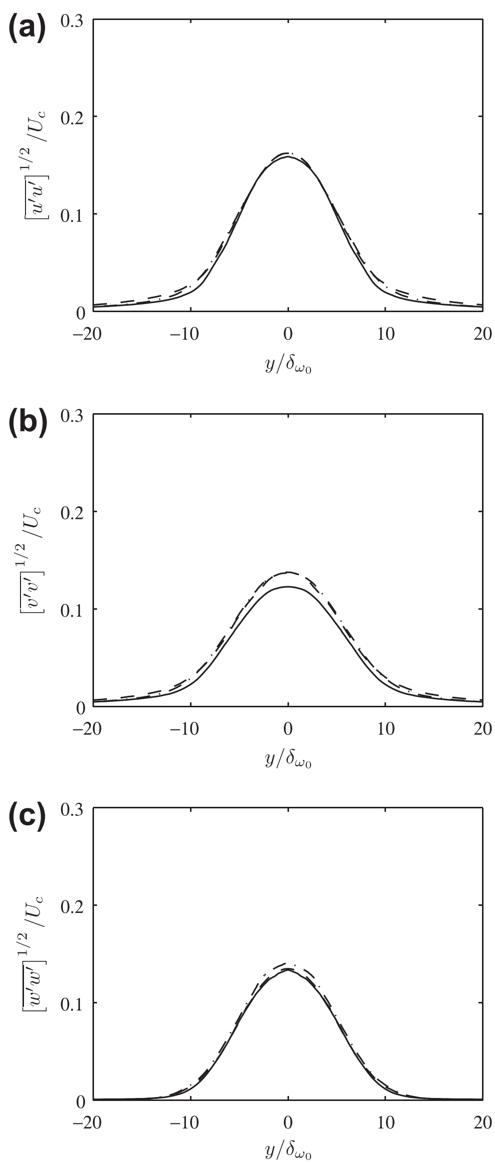

Fig. 12. Turbulent intensities as functions of the transverse location y/δ_{ω_0} at $x/\delta_{\omega_0} = 175$, for various discrete filters with adjusted mesh size to provide the same effective LES cut-off wavenumber. –.–.–, 6th-order; – – –, 8th-order; ——–, 10th-order. Turbulent intensities based on: (a) the streamwise, (b) the transverse, and (c) the spanwise velocity components.

5. Conclusion

The influence of the filter shape on compressible LES based on relaxation filtering has been investigated for a low-subsonic high-Reynolds number mixing layer. A reference solution in good agreement with experimental data found in the literature has first been obtained using high-order numerical algorithms. The impact of the order of the explicit discrete filter has then been studied by considering filters of order 2, 4, 6, 8 and 10. It appears that the 2nd-order filter is too dissipative and prevents the emergence of unsteady motions within the mixing layer. For higher order schemes, from 4th- to 10th-order, the flow solutions are turbulent, but exhibit statistics, namely mean flow and turbulent intensities, depending on the filter. The investigation of the one-dimensional kinetic energy spectra has demonstrated that the 4th-order filter may still be too dissipative whereas large scales remain unaffected using the 6th-, 8th- and 10th-order filters. The simulation results therefore seemed to depend on the filter shape. However, a further study of the kinetic energy spectra has shown that the effective spatial bandwidth of the LES increases with the order of the filter. It has been claimed that an appropriate comparison between LES data should be based on solutions having the same effective cut-off wavenumber. It turned out that simulations using the 6th-, 8th- and 10th-order filters, with mesh sizes chosen to yield the same effective LES cut-off wavenumber, provide similar results. The discrepancies between the flow statistics obtained using different filters are therefore found to be mainly related to the value of the effective LES cut-off wavenumber rather than to the filter shape itself. Filter shape independence is consequently achieved in the present LES of a mixing layer.

Acknowledgment

This work is supported by the "Agence Nationale de la Recherche" under the reference ANR-06-CIS6-011 (project "STURM4").

References

[1] Bell J, Mehta R. Development of a two-stream mixing layer from tripped and untripped boundary layers. AAIA J 1990;28:2034–42.
[2] Berland J, Bogey C, Bailly C. Low-dissipation and low-dispersion fourth-order Runge–Kutta algorithm. Comput Fluids 2006;35:1459–63.
[3] Berland J, Bogey C, Bailly C. Numerical study of screech generation in a planar supersonic jet. Phys Fluids 2007;19:075105.
[4] Berland J, Bogey C, Bailly C. Investigation using statistical closure theory of the influence of the filter shape on scale separation in large-eddy simulation. J Turbulence 2009;9:1–22.
[5] Berland J, Bogey C, Bailly C. A study of differentiation errors in large-eddy simulations based on EDQNM theory. J Comput Phys 2008;227(18):8314–40.
[6] Bogey C, Bailly C. A family of low dispersive and low dissipative explicit schemes for flow and noise computations. J Comput Phys 2004;194:194–214.
[7] Bogey C, Bailly C. Large eddy simulations of transitional round jets: influence of the Reynolds number on flow development and energy dissipation. Phys Fluids 2006;18:065101.
[8] Bogey C, Bailly C. Turbulence and energy budget in a self-preserving round jet: direct evaluation using large eddy simulation. J Fluid Mech 2009;627:129–60.
[9] Bogey C, Marsden O, Bailly C. Large-eddy simulation of the flow and acoustic fields of a Reynolds number 10^5 subsonic jet with tripped exit boundary layers. Phys Fluids, in press.
[10] Boris JP, Grinstein FF, Oran ES, Kolbe RL. New insights into large eddy simulation. Fluid Dyn Res 1992;10:199–228.
[11] Carati D, Winckelmans GS, Jeanmart H. On the modelling of the subgrid-scale and filtered-scale stress tensors in large-eddy simulation. J Fluid Mech 2001;441:119–38.
[12] De Stefano GD, Vasilyev OV. Sharp cutoff versus smooth filtering in large eddy simulation. Phys Fluids 2002;14(1):362–9.
[13] Domaradzki JA. Large eddy simulations without explicit eddy viscosity models. Int J Comput Fluid Dyn 2010;24(10):435–47.
[14] Emmert T, Lafon P, Bailly C. Numerical study of self-induced transonic flow oscillations behind a sudden duct enlargement. Phys Fluids 2009;21(2009):106105.
[15] Foysi H, Sarkar S. The compressible mixing layer: an LES study. Theor Comput Fluid Dyn 2010;24:565–88.
[16] Geurts BJ. Elements of direct and large-eddy simulations. Edwards; 2004.
[17] Ghosal S. An analysis of numerical errors in large-eddy simulations of turbulence. J Comput Phys 1996;125:187–206.
[18] Hickel S, Adams NA, Domaradzki JA. An adaptive local deconvolution method for implicit LES. J Comput Phys 2006;213(2):413–36.
[19] Leslie D, Quarini G. The application of turbulence theory to the formulation of subgrid modelling procedures. J Fluid Mech 1979;91:65–91.
[20] Mathew J, Lechner R, Foysi H, Sesterhenn J, Friedrich R. An explicit filtering method for large eddy simulation of compressible flows. Phys Fluids 2003;15(8):2279–89.
[21] Michalke A. On the inviscid instability of the hyperbolic-tangent velocity profile. J Fluid Mech 1964;19:543–56.
[22] Rizzetta DP, Visbal MR, Blaidell GA. Time-implicit compact differencing and filtering scheme for large-eddy simulation. Int J Numer Methods Fluids 2003;42(6):665–93.
[23] Sagaut P. Large-eddy simulation for incompressible flows. Scientific computation. Berlin: Springer; 2002.
[24] Smagorinsky JS. General circulation experiments with the primitive equations: I. the basic experiment. Mon. Weath. Rev. 1963;91:99–163.
[25] Stolz S, Adams NA. An approximate deconvolution procedure for large-eddy simulation. Phys. Fluids 1999;11(7):1699–701.
[26] Tam CKW, Dong Z. Radiation and outflow boundary conditions for direct computation of acoustic and flow disturbances in a nonuniform mean flow. J Comput Acoust 1996;4:175–201.
[27] Tantikul T, Domaradzki JA. Large eddy simulations using truncated Navier–Stokes equations with the automatic filtering criterion. J Turbulence 2010;11(21):1–24.
[28] Vasilyev O, Lund S, Moin P. A general class of commutative filters for LES in complex geometries. J Comput Phys 1998;146:82–104.
[29] Vreman B, Geurts B, Kuerten J. Subgrid-modelling in LES of compressible flow. Appl Sci J 1995;54:191–203.